



Full length article

Surface oxide and hydroxide effects on aluminum microparticle impact bonding



Jasper Lienhard^{a,1}, Cameron Crook^{b,1}, Maryam Zahiri Azar^b, Mostafa Hassani^{a,2}, Daniel R. Mumm^b, David Veysset^c, Diran Apelian^b, Keith A. Nelson^{c,d}, Victor Champagne^e, Aaron Nardi^e, Christopher A. Schuh^{a,*}, Lorenzo Valdevit^b

^a Department of Materials Science and Engineering, MIT, Cambridge, MA 02139, USA

^b Department of Materials Science and Engineering, University of California, Irvine, CA 92697, USA

^c Institute for Soldier Nanotechnologies, MIT, Cambridge, MA 02139 USA

^d Department of Chemistry, MIT, Cambridge, MA 02139 USA

^e U.S. Army Research Laboratory, Weapons and Materials Research Directorate, Aberdeen Proving Ground, MD, USA

ARTICLE INFO

Article history:

Received 19 April 2020

Revised 2 July 2020

Accepted 3 July 2020

Available online 9 July 2020

Keywords:

High-velocity impact

Cold spray

Oxide

Hydroxide

Critical adhesion velocity

ABSTRACT

Oxides, hydroxides, and other surface films act as impediments to metallurgical bonding during cold spray impact adhesion, raising the critical adhesion velocity and reducing the quality of the deposited coating. Using a single-particle impact imaging approach we study how altering the passivating surface oxides with exposures to various levels of heat and humidity affect the cold spray critical adhesion velocity in the case of aluminum. We analyze the thickness, composition and microstructure of the passivation layers with transmission electron microscopy (TEM), X-ray photoelectron spectroscopy (XPS), and Fourier-transform infrared spectroscopy (FTIR), and correlate our observations with a direct measurement of the critical adhesion velocity for each surface treatment. We conclude that exposures to temperatures as high as 300 °C for up to 240 min in dry air, or to room-temperature with humidity levels as high as 50% for 4 days, have negligible effect on the surface oxide layers, and by extension do not affect the critical adhesion velocity. In contrast, ambient-temperature exposure to 95% relative humidity levels for 4 days increases the critical adhesion velocity by more than 125 m/s, approximately a 14% percent increase. We observe that this distinct change in critical adhesion velocity is correlated with unique changes in the passivating layer thickness, thickness uniformity, crystallinity and composition resulting from exposure to high humidity. These results speak to particle surface treatments to improve the cold spray process.

© 2020 Acta Materialia Inc. Published by Elsevier Ltd. All rights reserved.

1. Introduction

Unlike other spray processes such as plasma spray or high-velocity oxy-fuel spray, the cold spray process does not require melting of the powder feedstock [1–4]. Particles are accelerated to supersonic speeds with a gas jet nozzle, impact a substrate, plastically deform, and bond to the substrate while remaining in the solid state. Particle impact velocities, which can be estimated through theoretical and experimental methods, are controlled by gas conditions, nozzle geometry, and particle characteristics [12]. Material build-up occurs when particles impact above a “critical

velocity”, a well-documented threshold speed required for solid-state microparticle adhesion [5,6]. Both this critical adhesion velocity, and the quality of the adhesion that occurs at impact velocities beyond it, are influenced by a range of variables including the material, angle of impact, and particle characteristics such as surface condition [5,7–11].

For metallic bonding to occur, clean and coherent metal contact at the atomic level is required. However, most metal surfaces oxidize in air at ambient temperature, forming a thin passivation film which may gradually thicken over time [13]. This native passivation layer, which exists on both the metal powder feedstock and the metal substrate, is believed to act as a barrier to metallurgical bonding and must be broken and displaced during cold spraying to create fresh metal-on-metal interfacial contact. Upon impact, cold spray particles deform and flatten rapidly, in the process forming jets of material at the particle-substrate interface [5,6,14–16]. Several researchers have suggested that this jetting phenomenon,

* Corresponding author.

E-mail address: schuh@mit.edu (C.A. Schuh).

¹ These authors contributed equally to this work.

² Current address: Sibley School of Mechanical and Aerospace Engineering, Cornell University, Ithaca, NY 14850, USA.

or the intense outward ejection of material around the edges of the particle during impact, is responsible for producing the necessary clean metal contact [5,17–20]. The large strains and extensive plastic deformation involved in jetting extrude material from both the particle and substrate, consequently disrupting the passivated surface films while pulling material towards the contact edge [3,6,8,20–23].

While models based on adiabatic shear instability [5,22,24,25] and hydrostatic pressure release [26–28] have been proposed to describe the onset of the jetting-bonding phenomenon, little quantitative work has been done to describe the importance of oxide break-up in cold-spray-induced bonding. Some empirical correlations between the oxygen content of the powder feedstock and the critical adhesion velocity have been previously reported. Studies by Kang et al. [29] and Li et al. [30], for example, reported that higher oxygen content in the powder feedstock is correlated with a higher critical adhesion velocity. Ko et al. [31] and Ichikawa and Ogawa [32] reported that changes in oxide chemistry or thickness can alter the cold spray deposition efficiency. Hassani-Gangaraj et al. [33] performed experiments comparing single-particle impact behavior between oxidizing and noble metals. They showed that jetting and bonding events appear similar between noble gold and oxidizing aluminum, and suggested, based on analysis of published cold spray data, that copper—a metal of intermediate nobility—has an oxide-dependent critical adhesion velocity. They did not, however, present single particle impact data on the same metal with different surface oxidation conditions in order to isolate the oxide-contribution to jetting or bonding.

In the present work, we use a similar single-particle impact imaging approach as that of Veysset et al. [34] to more explicitly isolate the effects of surface oxides and hydroxides on the critical adhesion velocity of high purity aluminum. By resolving the moment of impact with nanosecond level temporal resolution across a range of speeds, we precisely measure variation in the critical adhesion velocity caused by changes in particle surface characteristics, while keeping constant all other variables that would usually be uncontrollable and unclear in cold spray experiments, including particle size, shape, and instantaneous velocity and temperature at the time of impact. Using this approach, we measure the critical adhesion velocity for different sets of aluminum powders with variable surface oxide or hydroxide chemistries and thicknesses prepared with various heat and humidity treatments of the feedstock powders. Simultaneously, we correlate the impact observations directly with the composition, morphology, crystallinity, and thicknesses of the passivation layer observed to form with each heat/humidity treatment using high resolution transmission electron microscopy (TEM), X-ray photoelectron spectroscopy (XPS), and Fourier transform infrared spectroscopy (FTIR).

2. Experimental methods

2.1. Materials

The gas atomized aluminum powders used in this study were purchased from Valimet (Stockton, CA) and were processed at United Technologies Research Center (East Hartford, CT). Eight different sets of powders were produced with the same input materials, but with different treatments designed to affect the natively grown surface oxides. All treatments were conducted in fluidized bed reactors such as that shown in Fig. 1. One of these sets of powders was an “as-received” control sample with no additional thermal and environmental exposures. For three of the batches of powder, argon was fed into the fluidized bed reactor while the temperature was ramped to 300 °C at 10 °C / min. The powders were held at 300 °C for 30 min while the argon flow continued to allow the entire powder bed temperature to stabilize. Powders were

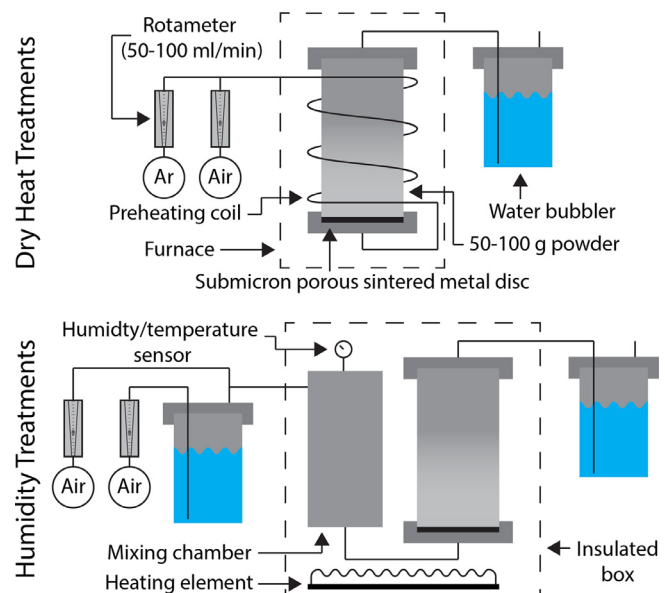


Fig. 1. Fluidized bed reactor schematics for high temperature and humidity treatments.

then held at 300 °C for an additional 240 min and then cooled under argon at 10 °C/min. During the 240 min hold the argon flow was replaced with dry air for three different lengths of time: 30, 60, and 240 min. The flow was then switched back to argon for the remainder of the hold. An additional control sample was also created, which followed the same cycles, but remained under argon flow the entire time. Two further batches of powders were processed in the reactor for four days at 29 °C with humidified air flowing at either 50% or 95% relative humidity, to represent some typical ambient storage conditions. Some of the powder processed in 95% relative humidity air was further heated to 300 °C for two hours in air, and then placed in a vacuum desiccator for four days to remove excess water from the surface. Table 1 summarizes the eight distinct batches of powder used in these experiments.

2.2. Characterization

2.2.1. X-ray photoelectron spectroscopy

Large area ($300 \times 700 \mu\text{m}$ slot aperture) X-ray photoelectron spectroscopy (XPS) spectra were collected on a Kratos AXIS Supra using an Al monochromatic X-ray source at 15 mA, an electron flood gun to reduce charging effects operated at 0.43 A, and a spectrum energy step size of 0.1 eV. Energy calibration was performed by adjusting the sp^2 bonded C 1 s peak to 284.5 eV. Due to the resolution of the instrument and the proximity of the characteristic (bonding-dependent) aluminum peaks, it was not possible to determine the chemical state of the constituents of the passivated aluminum system from XPS using either the O 2p or the Al 2p peaks [35,36]. XPS samples were prepared by densely packing powders on carbon tape affixed to a zirconia wafer used as a rigid substrate. Passivation layer thickness was measured from the XPS measurements following the procedure by Strohmeier [36], assuming a single uniform overlayer model via the formula:

$$d = \lambda_o \sin \theta \ln \left[\frac{N_m \lambda_m I_o}{N_o \lambda_o I_m} + 1 \right]$$

where d is the thickness of the passivation layer, λ is the inelastic mean free path of an electron (IMFP) in the given media, θ is the take-off angle (90° in the current instrument configuration), I is the corrected photoelectron peak areas (representing intensity), and subscripts m and o denote the Al 2p photoelectron peaks for

Table 1.

Name and description of processing protocols for eight different batches of powder, as well as critical adhesion velocity ranges for each batch of powder. The critical adhesion velocity ranges are defined for each set of powder as the range containing an equal number of bonding and non-bonding impacts with the fewest impacts required to ensure only one such range exists.

Name	Description	Critical Adhesion Velocity (m/s)
As-received powders (As-Recd)	No processing	[824 - 868]
High temperature baseline (HT-Base)	Ramped to 300 °C in argon and held in argon for 270 min	[801 - 827]
High temperature air 30 min (HT-30)	Ramped to 300 °C in argon, held in argon for 30 min, held in dry air for 30 min, held in argon for 210 min	[839 - 848]
High temperature air 60 min (HT-60)	Ramped to 300 °C in argon, held in argon for 30 min, held in dry air for 60 min, held in argon for 180 min	[787 - 843]
High temperature air 240 min (HT-240)	Ramped to 300 °C in argon, held in argon for 30 min, held in dry air for 240 min	[837 - 881]
50% relative humidity (RH-50)	50% relative humidity, 4-day exposure at 29 °C	[815 - 842]
95% relative humidity (RH-95)	95% relative humidity, 4-day exposure at 29 °C	[940 - 1001]
Desiccated 95% relative humidity (RH-95-D)	Identical treatment as RH-95 followed by dry heat treatment in air at 300 °C for 2 h then vacuum desiccation for 4 days	[864 - 940]

the metal and oxide respectively. Although this analysis is typically performed on flat substrates, we believe this method is applicable to the spherical powders studied here, considering that (1) the effective surface curvature is negligible within the analysis area defined by the aperture area, and (2) electrons emitted from the sides of the particles are heavily attenuated by small take-off angles relative to the particle surface and analyzer positioning.

Peak fitting was performed in a standardized processing software platform for XPS data (CasaXPS) using a Gaussian/Lorentzian peak shape (for peaks representing oxide and/or hydroxide) and a hybrid Doniach Sunjic and Gaussian/Lorentzian peak shape (for peaks representing the metal) [37]. The passivation layer was assumed to be primarily γ -Al₂O₃, because precise chemical information of the nature of the passivation layers was not known. Therefore, the IMFP in the oxide and metal were selected to be approximately 2.8 and 2.6 nm and the estimated ratio of $\frac{N_m}{N_o}$ was 1.5 [36].

2.2.2. Fourier-transform infrared spectroscopy (FTIR)

FTIR spectra were collected on a Jasco FT/IR-4700 spectrometer fitted with an Attenuated Total Reflectance (ATR) accessory, operated for wavenumbers in the range 800–4000 cm⁻¹. The instrument was equipped with a single bounce ATR accessory (ATR Pro One) with monolithic diamond, exhibiting a 1.0 cm⁻¹ resolution. Small quantities of the powder samples were placed atop the ATR diamond and held by a press against the surface during acquisition. Compositional identification was qualitatively performed via comparison with pure samples in Supplementary Fig. S2 and the OH stretching (~2800–4000 cm⁻¹) of the spectra.

2.2.3. Scanning/transmission electron microscopy

Thin lamellae comprising the passivating surface oxides and near-surface region of the metal particle were prepared by lift out from single particles (20–30 μ m in diameter) using focused ion beam (FIB) milling on a FEI Quanta 3D FEG (Thermo Fisher Scientific Inc.) dual beam (SEM/FIB). Particles were well dispersed on carbon tape affixed to the top of an SEM stub. A thin carbon protective layer was deposited by permanent marker to improve contrast during TEM/STEM imaging, and to protect specimen surfaces during subsequent platinum deposition. Platinum protective layers were deposited on top of the carbon film, first using an e-beam activated deposition followed by ion beam deposited platinum. The as-received, HT-240, and RH-95 samples were imaged on the JEOL JEM-2100F TEM operated at 200 kV. The RH-50 sample was imaged on the JEM-ARM300F Grand ARM TEM operated in STEM mode at 300 kV with spherical aberration correction.

2.3. Single particle impact measurements

In-situ single particle tests were conducted using an in-house-designed ballistic test apparatus described in more detail in Refs.

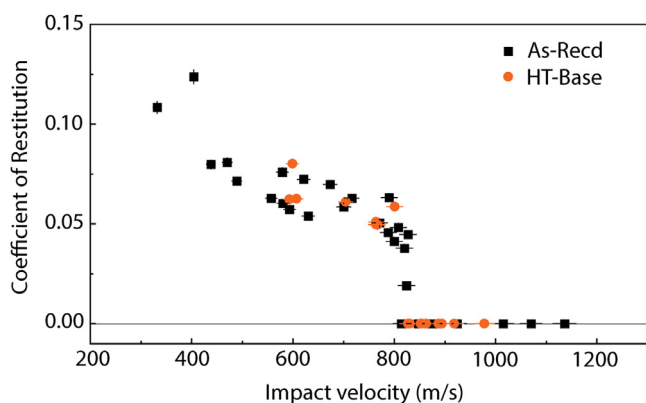


Fig. 2. Coefficient of restitution as a function of impact velocity for high temperature baseline and as-received control samples.

[17,34]. Powder particles were spread onto a launch pad comprising a glass substrate coated first with a sputtered gold film and then with a spin-coated polyurea film, atop which the particles were positioned. Individual particles were inspected and selected for launch using an optical microscope lens, and in this study all particles were selected to be spherical and $11 \pm 2 \mu\text{m}$ in diameter. A laser excitation pulse (pulsed Nd:YAG 10-ns duration, 532-nm wavelength) was then targeted at the back side of the launch pad, causing ablation of the gold layer and expansion of the elastomeric film behind the selected particle, launching it rapidly towards a 99.999% aluminum substrate (purchased from Laurand Associates Inc., Great Neck NY), polished to a mirror finish and positioned 750 μm away. Using a high-frame-rate camera (SIMX 16, Specialised Imaging), the in-flight velocity of the individual aluminum particle was recorded and the impact onto the substrate was observed. By using different laser pulse energies, multiple particles were launched, spanning a range of velocities. Particles launched at a velocity below the critical adhesion velocity rebounded off the substrate, and the post-impact rebound was recorded in addition to the initial inbound flight; from the video images the incident and rebound velocities could be recorded. All experiments were conducted in still air at room temperature.

The critical adhesion velocity is extracted from the raw data by aggregating results from many particle impact tests, as shown for example for the two control samples, as-received and HT-Base, in Fig. 2. Here the coefficient of restitution (the ratio of the rebound velocity to the impact velocity) is shown as a function of impact velocity. At lower velocities the particles rebound with nearly 10% of their incident velocity, but the coefficient of restitution decreases with increasing impact velocity until it reaches zero, indicating

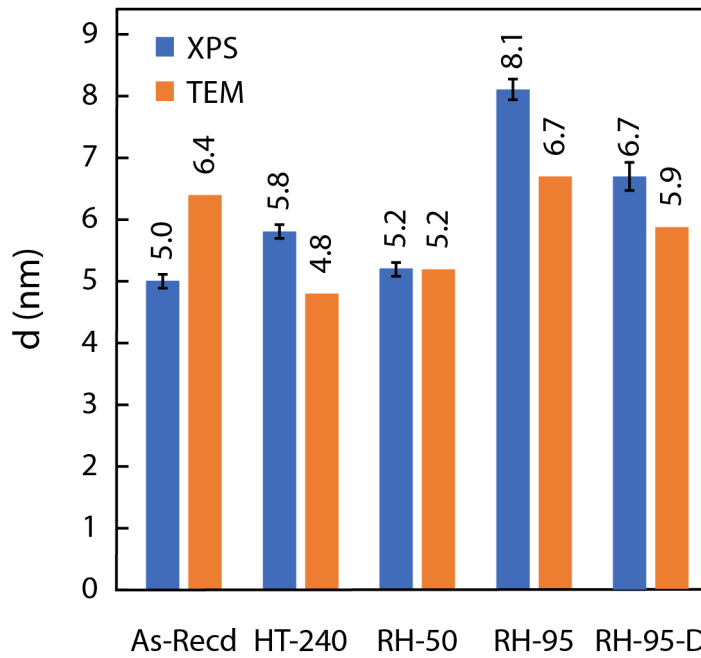


Fig. 3. Comparison of passivation layer thickness as determined from XPS and TEM.

cating that bonding has occurred. For pure metals this transition generally appears abruptly at nearly a single velocity [17], but alloying, surface effects, small differences in size or shape, etc. can introduce scatter into the critical adhesion velocity when it is measured using a series of individual particles. Accordingly, herein we report a narrow range of velocity values across which we observe some particles that bond and others that do not. This range is defined for each set of powders as the range of velocities containing an equal number of bonding and non-bonding impacts with the fewest impacts required to ensure only one such range exists. The average critical velocity is taken to be the average of the highest and lowest impact velocities reported in this range.

2.4. Post-mortem characterization

In order to observe cross sections of the impacted and adhered particles and the jets that form at the particle-substrate interface, bonded particles were micro-machined using a Helios Nanolab 600 Dual Beam Focused Ion Beam (FIB) Milling System at 30 kV accelerating voltage and currents ranging from 9.3 nA to 28 pA. An electron beam was used to deposit a thin layer of platinum on several of the adhered particles to protect the nanoscale jet features during the milling process.

3. Comparison of passivation layer thickness

Passivation layer thickness was measured by XPS and TEM. XPS utilized a large area aperture and thus the passivation layer thickness, as determined from the ratio of oxide and metallic Al 2p peak areas, is interpreted as an average over a powder sample encompassing a large number of particles. In contrast, TEM thickness measurements were performed on individual particles from which thin lamellas were lifted out, with each TEM micrograph only sampling a few tens of nanometers of oxide. Fig. 3 compares the oxide thickness of 5 different batches of powder, both extracted by XPS and averaged over TEM micrographs. Generally, we find reasonable agreement in the magnitude between XPS and TEM measurements, despite the assumptions made of the passivation layer composition and the round particle morphology

needed for the XPS analysis calculations. The discrepancies between the two measurement techniques are entirely attributed to the much smaller sample area of the TEM micrographs. While the agreement is generally within 1 nm, these discrepancies raise caution about extraction of thickness data from TEM images alone and support the use of XPS as a large-area technique. Therefore, comparison of passivation layer thickness is performed exclusively using the XPS calculated values in what follows. We emphasize that while their small measurement area does not provide reliable average thickness measurements, TEM micrographs do reveal rich data regarding the crystallinity, uniformity, and surface roughness of the oxide layers, which will be useful in the following sections.

4. Hot, dry air exposure

Fig. 4 shows high resolution TEM micrographs of the passivation layers of the as-received control sample (Fig. 4a) and the HT-240 sample (Fig. 4b) accompanied by XPS and TEM passivation layer thickness measurements of the as-received, HT-30, HT-60, and HT-240 samples (Fig. 4c,d). From the XPS thickness measurements, all the passivation layers were approximately ~5–6 nm, regardless of heat treatment duration or atmosphere (Fig. 4c). Confidence intervals based on the standard deviation of the XPS thickness measurements were approximately ± 0.2 – 0.3 nm as determined using the Monte Carlo computed error matrix, which approximates the relative sensitivity of the peak fitting to noise (see Supplementary information). In actuality, the errors may be somewhat higher considering the assumptions made of the IMFP, uniformity, composition, and curved particle surface. The passivation layer thicknesses from TEM micrographs were measured every 0.2 nm along the centerline from the intersection of the centerline normal with the boundaries formed from the carbon-passivation layer interface and the interior Al lattice. Distributions of passivation layer thickness for the as-received and the HT-240 samples are depicted in Fig. 4d, alongside their average values. The measured passivation layer thicknesses on these five samples are consistent with reported literature on low temperature oxidation of aluminum. Both the as-received and HT-240 sam-

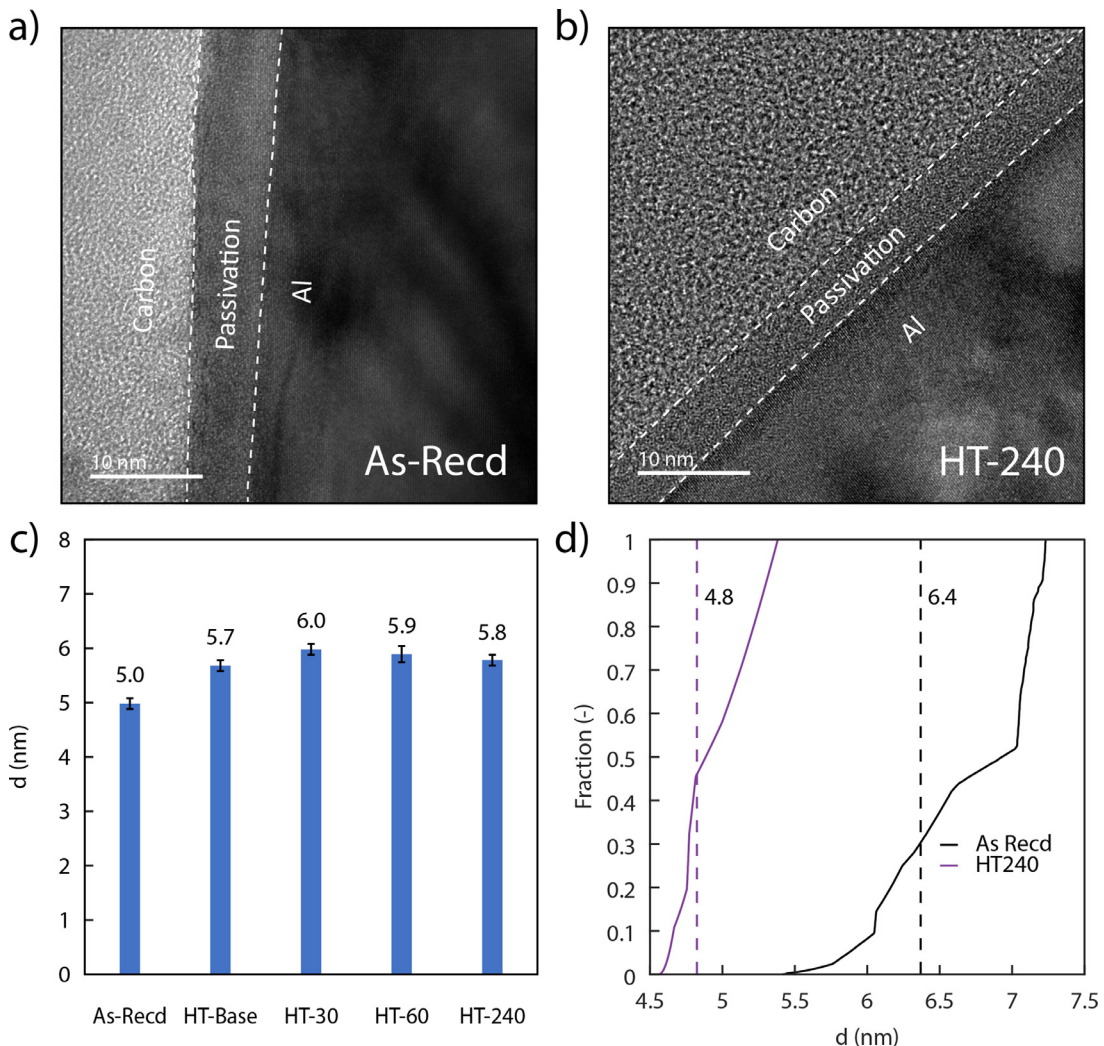


Fig. 4. TEM micrographs of surface passivation layers on the: (a) as-received; and (b) HT-240 sample. Dashed white lines denote the boundaries of the passivation layer in TEM micrographs. (c) XPS thickness measurements for control and hot and dry treated samples. (d) Cumulative distributions of measurements from the TEM micrographs of a and b with dashed line indicating the mean.

ples appear fully amorphous, uniform and smooth. Aluminum has been reported to form an amorphous oxide only a few nanometers thick at room temperature [38]. At oxidation temperatures less than 350 °C, the growth rate of this amorphous film is slow and logarithmic [39].

Thus, the first five samples listed in Table I are assessed to be essentially identical, in that they are the same base powder subjected to five treatments that apparently induce no substantive change in the surface characteristics of the powder. It is perhaps not surprising then to see that the single particle impact results in Fig. 5 show an excellent degree of overlap in the coefficient of restitution curves amongst these samples. There are two outliers in the 60- and 240-minute dry air samples at velocities near 1 km/s, for which we have no clear explanation, but when they are ignored the overlap of the five datasets is quite good and all exhibit critical adhesion velocities that are about the same. Table I also reports quantitative measures of the critical adhesion velocities; the ranges overlap amongst this series of samples.

On the premise that all five of these powders can be treated as chemically and structurally identical, we can aggregate all of the single particle impact data to give a more statistically robust range for the critical adhesion velocity of 836 ± 12 m/s. This value is only slightly different from the critical adhesion velocity of 810 m/s reported by Hassani-Gangaraj et al. [17], who used a single-particle

approach to measure the critical adhesion velocity of slightly larger aluminum particles $14 \pm 2 \mu\text{m}$ in diameter impacting an aluminum substrate, with an unknown surface condition that we assume would be rather like our as-received powders.

5. Humid air exposure

Fig. 6 shows high resolution TEM/STEM images of the surfaces of the 50% (Fig. 6a) and 95% (Fig. 6b,c) relative humidity exposure samples, alongside thickness measurements (Fig. 6d) and distributions (Fig. 6e) obtained by TEM and XPS. Despite exposure to humidity, the passivation layer of the RH-50 sample was not observed to thicken. However, noticeable surface roughening is observed and likely indicates the beginning of hydration of the outermost surface [40]. Nonetheless, the passivation layer appears to remain amorphous. In contrast, the RH-95 sample has noticeably thickened compared to the high temperature and dry treated samples, but the surface appears to be smooth unlike the RH-50 sample – with the caveat of significantly greater thickness variations of approximately 3.5 nm. Furthermore, pockets of crystallinity were observed within the passivation layer of the RH-95 sample as denoted in Fig. 6c. Though the passivation layer on these powders is approximately 8 nm thick on average, only slightly thicker in an absolute sense than that of both the control sample and RH-50

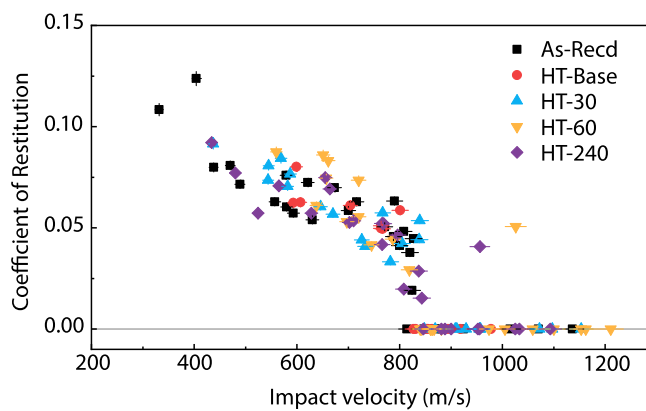


Fig. 5. Coefficient of restitution as a function of impact velocity for as-received powder, high temperature baseline, 30 min at 300 °C, 60 min at 300 °C, and 240 min at 300 °C.

samples at ~5–6 nm, this represents a significant relative increase in thickness of ~45%.

Fig. 7 shows the measured FTIR spectra for seven treated samples. The only sample to show clear evidence of OH groups is the RH-95 sample, as seen from strong characteristic OH stretching vibrational mode peaks between 3300 and 3700 cm⁻¹ – which coincide with several of the polymorphs of aluminum hydroxides and oxyhydroxides, specifically gibbsite, diaspore, and bayerite [41,42]. Interestingly, these spectra exclude the presence of boehmite and perhaps nordstrandite (see Supplementary information, Fig. S2).

Fig. 8 shows the single-particle impact test results for each batch of powder exposed to humid air, as well as a control batch, while Table I reports the measured critical adhesion velocities. We did not observe a significant difference in critical adhesion velocity between the as-received particles and the 50% relative humidity particles, with both lying in the range of ~815 to 860 m/s. However, with the 95% relative humidity powders we observe a significant jump in the critical adhesion velocity to ~970 m/s. The fact that this is the only specimen group to show any deviation in the critical adhesion velocity matches well with the fact that this was the only sample to exhibit unique surface features, including: (1) a passivation layer that on average was slightly thicker (~8 nm) than found with both the control sample and the 50% relative humidity powder (~5 nm); (2) distinct regions of crystallinity in the oxide/hydroxide on the 95% powder; and (3) the presence of OH bonds, with spectral features associated with crystalline forms of the oxides/hydroxides in the spectrum – not seen in the other samples.

Any or all of the differences observed between the passivation layer on the RH-95 sample and the as-received powder may contribute to the observed increase in critical adhesion velocity in that single batch of powder. In an attempt to deconvolve the respective roles of these changes, we conducted an additional set of experiments in which we attempted to dehydrate these powders by heating and desiccating them. A small amount of the 95% relative humidity powder was heated to 300 °C for two hours, and then placed in a vacuum desiccator for four days with the goal of removing as much hydration from the surface of the particles as possible. Based on our observation above that passivation layer structure and critical adhesion velocity was not affected by holding as-received powder at 300 °C in a dry or low relative humidity environments for several hours, this heating and desiccation treatment was designed as an effort to remove excess hydration from the surface of the particles without otherwise growing the native oxide.

Following heat treatment and vacuum desiccation, the passivation layer of the RH-95-D sample was observed to decrease in thickness slightly, by less than a nm, and recover a higher degree of thickness uniformity. There was no evidence of crystallinity within the passivation layer after the treatment as seen in **Fig. 9**. The absence of strong peaks in the FTIR spectra following desiccation [43] indicates some recovery of a metastable oxide form; however, the broad peak centered at 3300 cm⁻¹ may partially be the result of remaining physisorbed water [42]. Therefore, we conclude the pockets of crystallinity within the RH-95 sample were likely alumina (oxy)hydroxides, which are apparently lost upon dehydration. Again, from the TEM micrographs of **Fig. 9**, the passivation layer of the desiccated powder remains smooth and varies in thickness less than the RH-95 sample.

We then retested the impact and bonding behavior post-desiccation, with results shown in **Fig. 10**. Interestingly, we did in fact observe a drop in the velocity required for adhesion in the desiccated powders. While there is more scatter in this new dataset than in the others (a point to which will we shortly return), quantitatively, the average critical adhesion velocity declined from 970 to 902 m/s, and the lowest velocity at which we recorded an adhesion event dropped from 955 to 879 m/s.

6. Discussion

Multiple differences were observed between the passivation layer on the RH-95 sample and the as-received powder: the thickness, composition, and microstructure are all affected by the high-humidity treatment, where none of the other treatments induced changes in any of those properties of the passivation layer. The data on the desiccated, dried 95% relative humidity powder provided evidence that hydroxide chemistry, and in particular the presence of OH, seems to be an important factor in determining the critical adhesion velocity. This set of powders displayed a critical adhesion velocity that was less well defined than the other batches of powders. In other words, there was a range of velocities, roughly between 870 and 1000 m/s, in which a mixture of both adhesion and rebound behavior was observed. This result shows that the surface chemistry changes caused by moisture may involve subtle and variable effects from one particle to the next.

In addition to changes in chemistry, a three-nanometer difference in oxide thickness was observed between the as-received and the RH-95 powder. On its face, 3 nm of additional oxide thickness seems rather insignificant to the scale of the problem of impact adhesion, with its 10 µm particle-size scale and associated large plastic zone size. However, we note that the controlling physics of bonding has been related to the formation of extremely small 'jets' of ejected material at the periphery of the particle contact region, locations which inherently involve the passivation oxides. As such, the relative importance of the surface passivation layer to these very small jets may be much higher. We explore this notion in what follows.

In 2005 Vlcek et al. provided a qualitative ranking of material suitability for the cold spray process based on shock-compression phenomena and related physical effects, such as impact heating and dynamic yielding [44]. These researchers suggested that critical adhesion velocity and the onset of jetting are closely related to shock-compaction phenomena in matter. More recently, hydrodynamic pressure release has been proposed as the mechanism controlling the onset of jetting and bonding in cold spray by Hassani-Gangaraj et al. [26,27]. When a high-speed microparticle first impacts a substrate, a compressed shock wave is formed at the contact interface. A few nanoseconds later, the high-pressure wave overtakes and detaches from the edge of the flattening particle, releasing the pressure at the free surface and producing significant localized tension; this leads to spall/fragmentation in the form

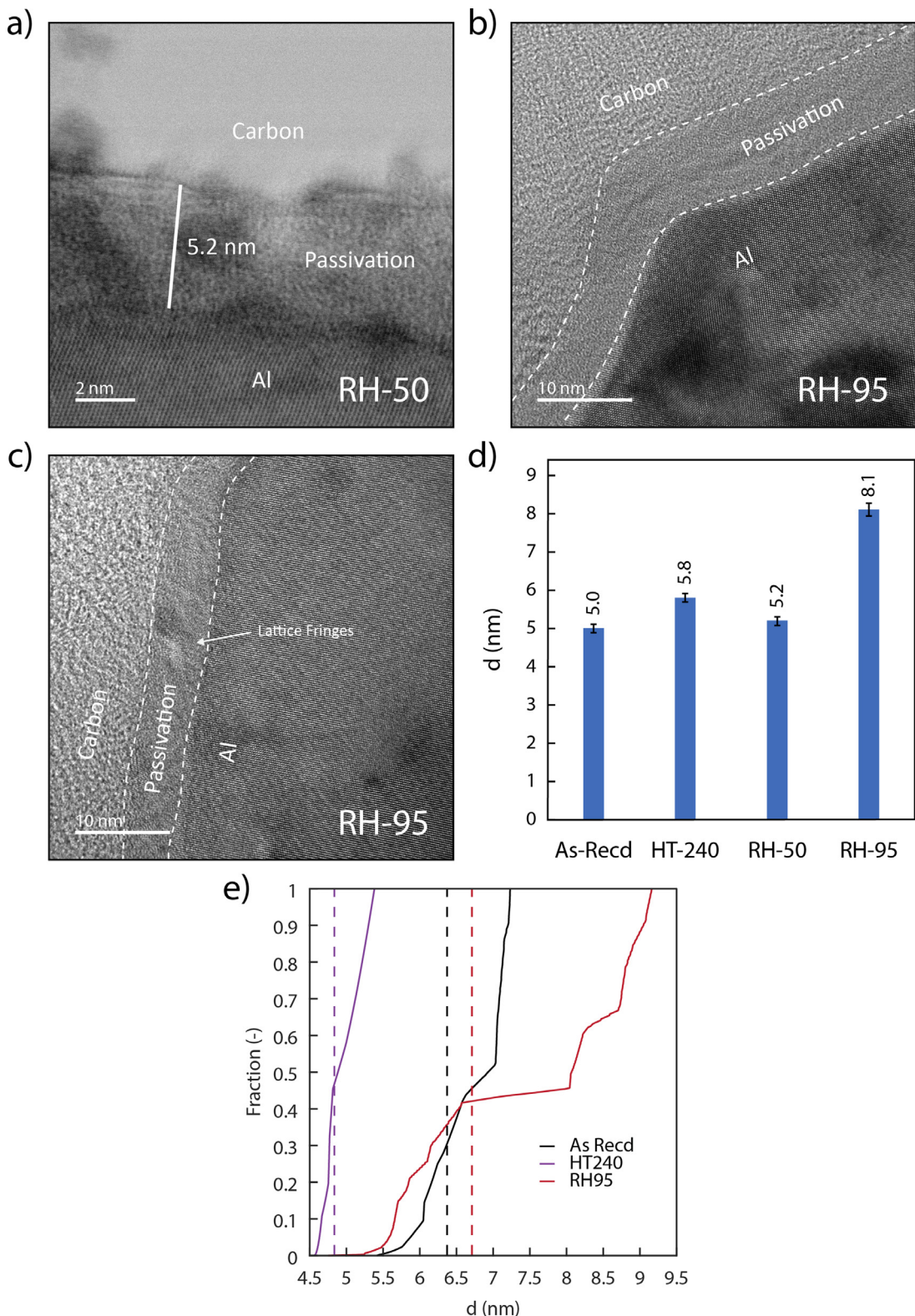


Fig. 6. (a) High resolution dark field STEM of the 50% relative humidity exposure and (b,c) high resolution TEM of the 95% relative humidity exposure passivation layers. Dashed white lines denote the boundaries of the passivation layer in TEM micrographs. (d) XPS thickness measurements of all aluminum samples show the high humidity is the only sample to noticeably thicken. (e) Cumulative distributions of measurements of TEM micrographs for as-received, HT-240, and RH-95 samples. Dashed lines indicate the mean. The RH-95 sample exhibits a much broader variation in thickness with significantly thicker regions. The RH-50 sample is omitted from the cumulative distribution because of the significantly higher magnification and thus smaller sampling region.

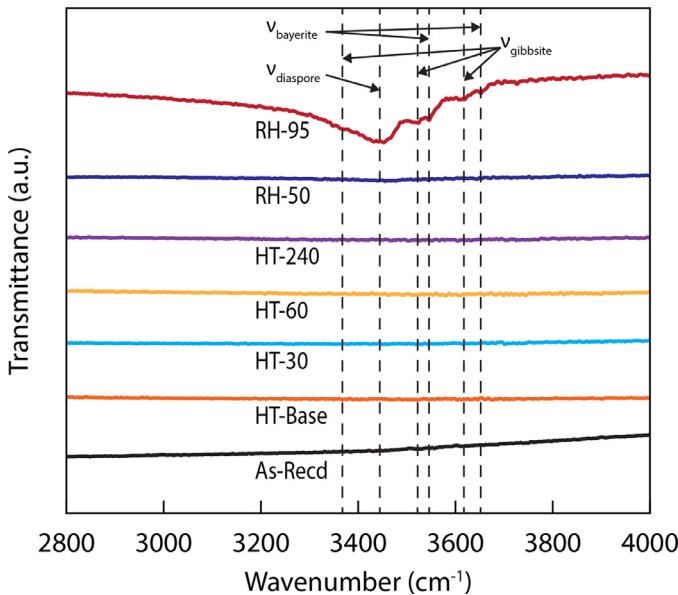


Fig. 7. Fourier-transform infrared spectra of high purity aluminum powder samples shows that the only sample with the presence of OH stretching vibration modes is the RH-95 sample.

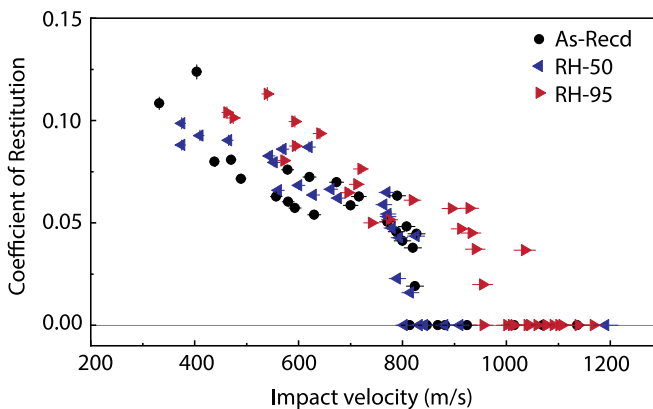


Fig. 8. Coefficient of restitution as a function of impact velocity for as-received powder, 50% relative humidity powder, and 95% relative humidity powder.

of a jet. It is widely believed in the field of cold spray that such localized deformation precisely at the interfacial regions between particle and substrate is responsible for the break-up of passivation layers, allowing clean metal contact and bonding to occur [3,6,8,20–22]. A schematic of jet formation is shown in Fig. 11,

where we also illustrate the oxide or hydroxide layer; although the oxide is small compared to the particle, it is more significant on the scale of the jets, which are very fine, having nanoscale features.

Fig. 12a shows an image of the particle-substrate interface on an as-received particle which impacted the substrate at approximately 900 m/s. Jetted material can clearly be seen extending out from the interface and folding over onto the substrate. As the jetted material tends to fold over on itself, understanding the thickness of the jets by looking down from above is difficult. Instead, Fig. 12b, 12c, and 12d show cross-sections of impacted particles that have been milled with a focused ion beam. Fig. 12b shows a FIB cross section of the jet on an impacted as-received particle, focused on the right-hand side of the particle and cut through its center. Here we see the dome of the particle and the interface between the particle and substrate, with an ejected jet of material emerging where the interface meets the free surface. Fig. 12c shows an impacted and bonded RH-95 cross-sectioned particle, and Fig. 12d shows a higher magnification image of the same particle focused on the right-hand side. Although the jet in Fig. 12c and 12d is covered with Pt (used as a protective coating during ion milling), we can easily discern the jetted aluminum, indicated with white arrows, which is at most 300 nm thick. The tip of the post-mortem remaining jet material has a thickness on the order of 100 nanometers. In Fig. 12, the jet appears to come preferentially from the substrate side of the interface. There were no significant observable differences in the postmortem impacts of the as-received aluminum powder and the RH-95 powder.

The extremely fine size of the jetted region supports the observation that just a few nanometers of oxide material can have a pronounced effect on impact bonding, and explains the role of humidity through its inflation of the thickness of that layer and modification of the local mechanical characteristics. A simple estimate of these roles can be made using Hassani-Gangaraj et al.'s model for jet formation based on hydrodynamic pressure release, which suggests that the critical adhesion velocity for jetting is proportional to the dynamic yield strength (or spall strength) of the material [26,45]. To a first order approximation, the geometry of the jet is roughly one of simple parallel tensile loading of both metal and oxide (as shown schematically in Fig. 11b), and we imagine that just beneath the surface of the particle and substrate contact edge is a state of nearly pure tension parallel to the interface back to at least some distance away from the particle and substrate contact edge. This geometry is such that the oxide layer can have a large influence: in the limit of pure interfacial tension, a simple rule-of-mixtures on the dynamic strengths of aluminum and aluminum oxide might control the formation of a jet, where the oxide, being a more rigid and nominally stronger reinforcing layer, would increase the “effective” strength at the interface. A natural consequence of strengthening the interface in this way is that the

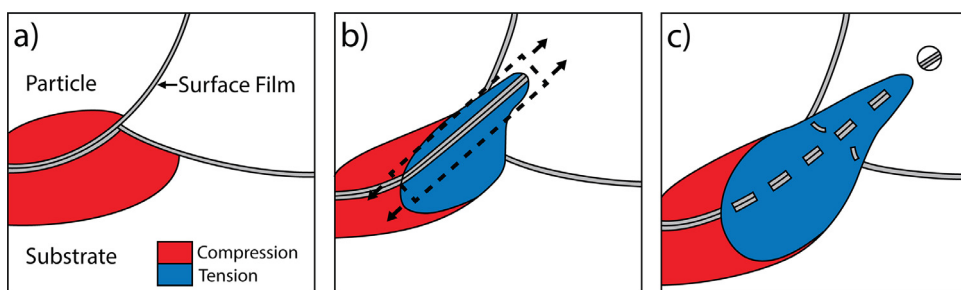


Fig. 11. Sequence of events during jetting. a) Upon impact, a shock wave is induced. b) Several nanoseconds later, the shock wave detaches from the leading edge of the particle-substrate interface, releasing pressure at the free surface and creating a region of localized tension. c) When this localized tension exceeds the effective spall strength of the material in the jet, the material will accelerate, and a jet will form. The thickness of the oxide is exaggerated in this illustration, and the uniformity of the colors is not meant to suggest that pressure/tension is uniformly distributed. More of the jet material appears to originate in the substrate than in the particle.

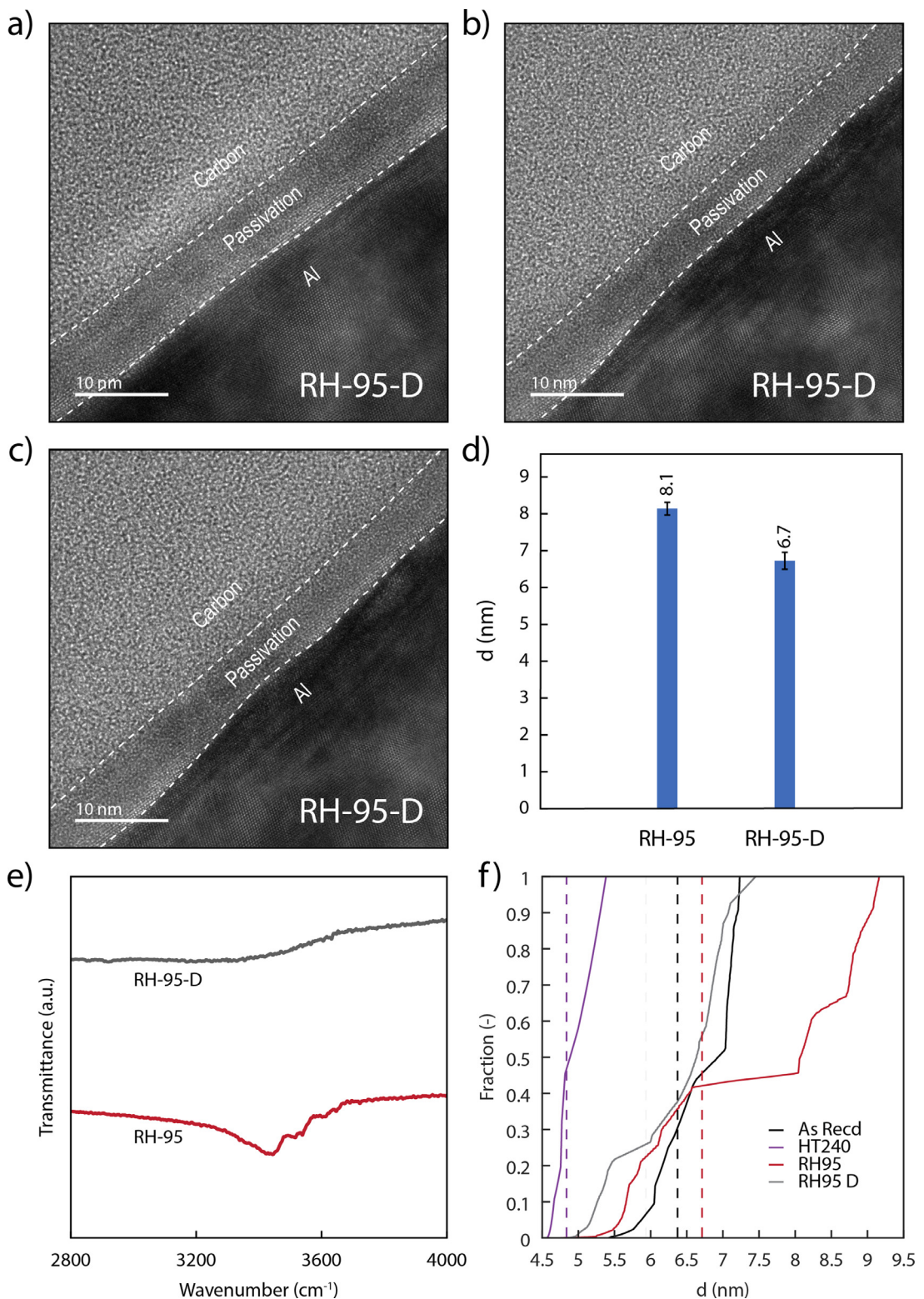


Fig. 9. (a,b,c) Three high resolution micrographs taken from a desiccated 95% relative humidity exposure particle after heat treatment and desiccation, to show the range of thicknesses typically observed. Dashed white lines denote the boundaries of the passivation layer in TEM micrographs. (d) XPS thickness measurements show excellent agreement with TEM measurements. (e) FTIR spectra show the disappearance of OH stretching modes post treatment indicating recovery of a metastable oxide form. The broad band at 3300 cm^{-1} may indicate remaining surface physisorbed water. (f) The cumulative distribution of thickness measurements. The desiccated sample shows a similar distribution to the as-received sample.

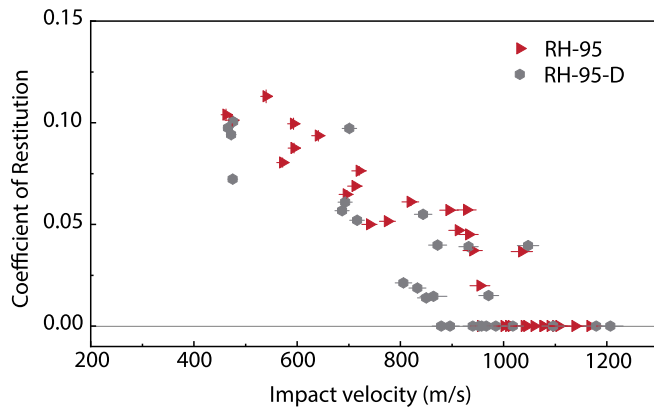


Fig. 10. Coefficient of restitution as a function of impact velocity for the 95% relative humidity particles and desiccated 95% relative humidity particles.

amount of strain that develops would be reduced; as seen in, e.g., cold pressure welding [46]. Lower interfacial strains would affect not only the area of broken oxide through which metallic bonds could form, but also the formation of metal-on-metal contacts by extrusion through available oxide gaps.

Taking 100 nanometers as the total cross-sectional width of the initial jet region, the passivating oxide layer would represent about 5% of the thickness in as-received materials and a bit more at 8% in the RH-95 powder. Given that spall strength is proportional to bulk modulus, the ratio of oxide to aluminum strength is of the order 2x for an amorphous oxide and 3x for a semi-crystalline oxide. A simple parallel-loading rule-of-mixtures using these kinds of inputs can plausibly support an increase in critical adhesion velocity of about 15% upon our RH-95 treatment, which thickens the oxide

by 3 nm and creates pockets of crystallinity in the oxide, with an associated increase in the effective oxide strength. This increase is rather comparable to the measured 14% increase in critical adhesion velocity with the RH-95 treatment.

Thus, while it is nominally surprising that a few nanometers of passivating oxide could affect impact bonding by over 100 m/s in critical adhesion velocity, the nature of the severe local deformation that prevails at the interface dramatically inflates the relevance of that layer's geometry and properties. We therefore propose that particle surface treatments that impact surface chemistry and phases should be more actively explored as a potentially fruitful avenue for improved cold spray coatings.

7. Conclusion

In order to understand the role of surface oxides/hydroxides in cold spray adhesion, we measured the critical adhesion velocity for eight batches of aluminum powders that had been processed in different humidity and temperature environments. Heating aluminum powder to a temperature of up to 300 °C for a finite amount of time of less than 4 h caused no observable changes in the surface condition of the powders that we identified using our characterization methods, and no significant change in the critical adhesion velocity. In contrast, a batch of aluminum powder that was held in 95% relative humidity room temperature air for four days exhibited a dramatic 14% jump of more than 125 m/s in critical adhesion velocity. Using several characterization techniques including transmission electron microscopy and X-ray photoelectron spectroscopy, we observed that the thickness of the passivation layer on this high-humidity powder had increased by about 2–3 nm. Furthermore, changes in the surface chemistry were observed, with the hydrated powders containing OH bonds that were not present in the control samples and suggestions of greater crys-

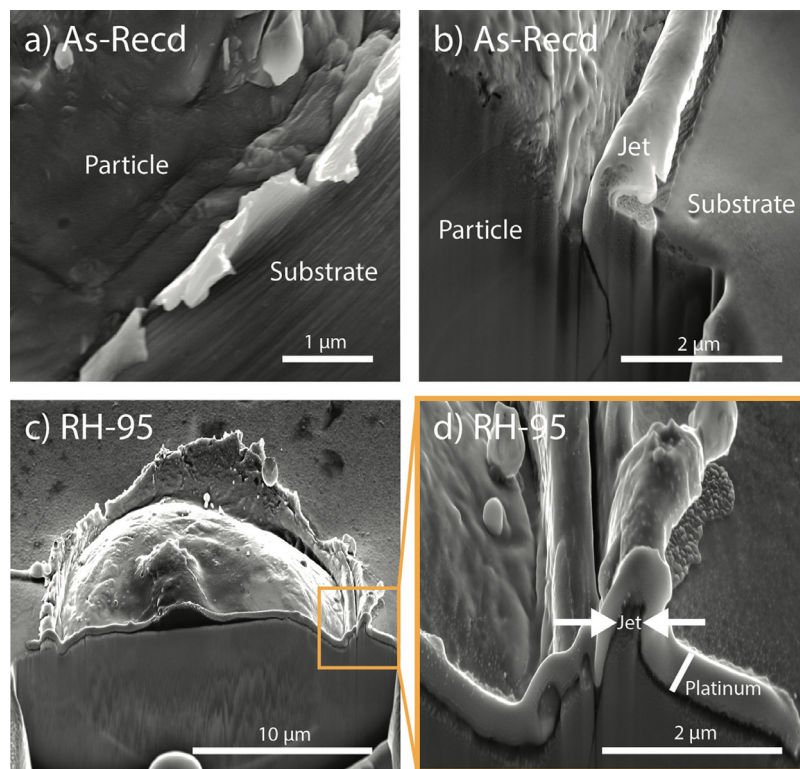


Fig. 12. (a) Particle-substrate interface of an as-received particle, (b) postmortem remains of a jet on an impacted as-received particle, (c) cross-section of an impacted RH-95 particle, (d) and closer view of RH-95 cross-section.

tallinity as well. A second experiment retested the critical adhesion velocity of these high-humidity particles after desiccation, which resulted in a reduction of critical adhesion velocity (with attendant reductions in observed hydration and crystallinity), but not a full recovery to that of the control sample.

Based on these experiments, we conclude that the nature of the passivation layer—its thickness, chemistry and structure—can contribute significantly to impact adhesion. While it is notionally somewhat unexpected that 3 nm of growth in a passivation layer can affect impact bonding to such a large degree, we find that it can be rationalized on the basis of how localized the interface deformation leading to bonding is. Our measurements of impact jetting at the contact periphery suggest localization to a level of ~100 nm, which renders a change in the passivating layer thickness at the scale of just a few nanometers surprisingly relevant, especially when the layer hydrates and crystallizes as well.

The changes in critical adhesion velocity we observed on exposure to humid air suggest that the environment powder is stored in can have important consequences in industrial cold spray processing. Storing powder feedstock in humid environments, for example, may significantly reduce the quality of the powder and significantly raise the critical adhesion velocity. In contrast, storing powder in hot dry air should be less problematic. In the future, particle surface treatments should be considered a key direction for improving cold spray processes. Further work will be required to further quantify the role of passivation layer thickness on critical adhesion velocity when no changes in chemistry or hydration are present. Methods for reducing or removing surface oxides/hydroxides and contamination should also be explored as they may lead to reductions in critical adhesion velocity required for cold spray adhesion.

Declaration of Competing Interest

The authors declare that they have no known competing financial interests or personal relationships that could have appeared to influence the work reported in this paper.

Acknowledgements

CC, MZA, DA, DRM and LV acknowledge support from the U.S. Army Research Laboratory (contract #W911NF-15-2-0024) via a subcontract from Worcester Polytechnic Institute. SEM, FIB, TEM, and STEM work was performed at the UC Irvine Materials Research Institute (IMRI), using instrumentation funded in part by the National Science Foundation Center for Chemistry at the Space-Time Limit (CHE-082913). FTIR measurements were conducted at the UCI Laser Spectroscopy Lab. JL, MH, DV, KN, and CS acknowledge support from the U.S. Army Research Laboratory (contract #W911NF-15-2-0026) under subcontract from Northeastern University. *In-situ* particle impact experiments were performed at the MIT Institute for Soldier Nanotechnology. Postmortem FIB and SEM characterization of particle impacts was performed at the MIT Materials Research Laboratory.

References

- [1] V.K. Champagne (Ed.), *The Cold Spray Materials Deposition Process*, Woodhead Publish, Cambridge, UK, 2007.
- [2] A.P. Alkhimov, V.F. Kosarev, A.N. Papyrin, Gas-dynamic spraying. An experimental study of the spraying process, *J. Appl. Mech. Tech. Phys.* 39 (1998) 318–323, doi:10.1007/bf02468100.
- [3] R.C. Dykhuizen, M.F. Smith, D.L. Gilmore, R.A. Neiser, X. Jiang, S. Sampath, Impact of high velocity cold spray particles, *J. Therm. Spray Technol.* 8 (1999) 559–564, doi:10.1361/105996399770350250.
- [4] M. Hassani-Gangaraj, D. Veysset, K.A. Nelson, C.A. Schuh, Melting Can Hinder Impact-Induced Adhesion, *Phys. Rev. Lett.* 119 (2017) 1–5, doi:10.1103/PhysRevLett.119.175701.
- [5] H. Assadi, F. Gärtner, T. Stoltenhoff, H. Kreye, Bonding mechanism in cold gas spraying, *Acta Mater.* 51 (2003) 4379–4394, doi:10.1016/S1359-6454(03)00274-X.
- [6] T. Schmidt, F. Gärtner, H. Assadi, H. Kreye, Development of a generalized parameter window for cold spray deposition, *Acta Mater.* 54 (2006) 729–742, doi:10.1016/j.actamat.2005.10.005.
- [7] F. Raletz, M. Vardelle, G. Ezoo, Critical particle velocity under cold spray conditions, *Surf. Coatings Technol.* 201 (2006) 1942–1947, doi:10.1016/j.surfcoat.2006.04.061.
- [8] C.J. Li, W.Y. Li, H. Liao, Examination of the critical velocity for deposition of particles in cold spraying, *J. Therm. Spray Technol.* 15 (2006) 212–222, doi:10.1361/105996306X108093.
- [9] R.Z. Huang, H. Fukanuma, The influence of spray conditions on deposition characteristics of aluminum coatings in cold spraying, *Proc. Int. Therm. Spray Conf.* (2009) 279–284, doi:10.1361/cp2009itsc0279.
- [10] Y. Watanabe, C. Yoshida, K. Atsumi, M. Yamada, M. Fukumoto, Influence of Substrate Temperature on Adhesion Strength of Cold-Sprayed Coatings, *J. Therm. Spray Technol.* 24 (2014) 86–91, doi:10.1007/s11666-014-0165-3.
- [11] W. Sun, A.W.Y. Tan, A. Bhowmik, I. Marinescu, X. Song, W. Zhai, F. Li, E. Liu, Deposition characteristics of cold sprayed Inconel 718 particles on Inconel 718 substrates with different surface conditions, *Mater. Sci. Eng. A* 720 (2018) 75–84, doi:10.1016/j.msea.2018.02.059.
- [12] V.K. Champagne, D.J. Helfritch, S.P.G. Dinavahi, P.F. Leyman, Theoretical and experimental particle velocity in cold spray, *J. Therm. Spray Technol.* 20 (2011) 425–431, doi:10.1007/s11666-010-9530-z.
- [13] R.E. Smallman, *Modern Physical Metallurgy*, Butterworth-Heinemann, 2017.
- [14] P.C. King, G. Bae, S.H. Zahiri, M. Jahedi, C. Lee, An experimental and finite element study of cold spray copper impact onto two aluminum substrates, *J. Therm. Spray Technol.* 19 (2010) 620–634, doi:10.1007/s11666-009-9454-7.
- [15] T. Liu, J.D. Leazer, L.N. Brewer, Particle deformation and microstructure evolution during cold spray of individual Al–Cu alloy powder particles, *Acta Mater.* 168 (2019) 13–23, doi:10.1016/j.actamat.2019.01.054.
- [16] M.V. Vidaller, A. List, F. Gaertner, T. Klassen, S. Dosta, J.M. Guilemany, Single Impact Bonding of Cold Sprayed Ti-6Al-4V Powders on Different Substrates, *J. Therm. Spray Technol.* 24 (2015) 644–658, doi:10.1007/s11666-014-0200-4.
- [17] M. Hassani-Gangaraj, D. Veysset, K.A. Nelson, C.A. Schuh, In-situ observations of single micro-particle impact bonding, *Scr. Mater.* 145 (2018) 9–13, doi:10.1016/j.scriptamat.2017.09.042.
- [18] P.C. King, C. Busch, T. Kittel-Sherri, M. Jahedi, S. Gulizia, Interface melding in cold spray titanium particle impact, *Surf. Coatings Technol.* 239 (2014) 191–199, doi:10.1016/j.surfcoat.2013.11.039.
- [19] Y. Ichikawa, R. Tokoro, M. Tanno, K. Ogawa, Elucidation of cold-spray deposition mechanism by auger electron spectroscopic evaluation of bonding interface oxide film, *Acta Mater.* 164 (2019) 39–49, doi:10.1016/j.actamat.2018.09.041.
- [20] M. Grujicic, J.R. Saylor, D.E. Beasley, W.S. DeRosset, D. Helfritch, Computational analysis of the interfacial bonding between feed-powder particles and the substrate in the cold-gas dynamic-spray process, *Appl. Surf. Sci.* 219 (2003) 211–227, doi:10.1016/S0169-4332(03)00643-3.
- [21] W.Y. Li, C.J. Li, H. Liao, Significant influence of particle surface oxidation on deposition efficiency, interface microstructure and adhesive strength of cold-sprayed copper coatings, *Appl. Surf. Sci.* 256 (2010) 4953–4958, doi:10.1016/j.apsusc.2010.03.008.
- [22] M. Grujicic, C.L. Zhao, W.S. DeRosset, D. Helfritch, Adiabatic shear instability based mechanism for particles/substrate bonding in the cold-gas dynamic-spray process, *Mater. Des.* 25 (2004) 681–688, doi:10.1016/j.matdes.2004.03.008.
- [23] W.Y. Li, H. Liao, C.J. Li, G. Li, C. Coddet, X. Wang, On high velocity impact of micro-sized metallic particles in cold spraying, *Appl. Surf. Sci.* 253 (2006) 2852–2862, doi:10.1016/j.apsusc.2006.05.126.
- [24] G. Bae, Y. Xiong, S. Kumar, K. Kang, C. Lee, General aspects of interface bonding in kinetic sprayed coatings, *Acta Mater.* 56 (2008) 4858–4868, doi:10.1016/j.actamat.2008.06.003.
- [25] G. Bae, S. Kumar, S. Yoon, K. Kang, H. Na, H.J. Kim, C. Lee, Bonding features and associated mechanisms in kinetic sprayed titanium coatings, *Acta Mater.* 57 (2009) 5654–5666, doi:10.1016/j.actamat.2009.07.061.
- [26] M. Hassani-Gangaraj, D. Veysset, V.K. Champagne, K.A. Nelson, C.A. Schuh, Adiabatic shear instability is not necessary for adhesion in cold spray, *Acta Mater.* 158 (2018) 430–439, doi:10.1016/j.actamat.2018.07.065.
- [27] M. Hassani-Gangaraj, D. Veysset, K.A. Nelson, C.A. Schuh, Supersonic Impact of Metallic Micro-particles, *ArXiv* 1612.08081. (2016).
- [28] S. Suresh, S.W. Lee, M. Aindow, H.D. Brody, V.K. Champagne, A.M. Dongare, Mesoscale modeling of jet initiation behavior and microstructural evolution during cold spray single particle impact, *Acta Mater.* 182 (2020) 197–206, doi:10.1016/j.actamat.2019.10.039.
- [29] K. Kang, S. Yoon, Y. Ji, C. Lee, Oxidation dependency of critical velocity for aluminum feedstock deposition in kinetic spraying process, *Mater. Sci. Eng. A* 486 (2008) 300–307, doi:10.1016/j.msea.2007.09.010.
- [30] C.J. Li, H.T. Wang, Q. Zhang, G.J. Yang, W.Y. Li, H.L. Liao, Influence of spray materials and their surface oxidation on the critical velocity in cold spraying, *J. Therm. Spray Technol.* 19 (2009) 95–101.

- [31] K.H. Ko, J.O. Choi, H. Lee, B.J. Lee, Influence of oxide chemistry of feedstock on cold sprayed Cu coatings, *Powder Technol.* 218 (2012) 119–123, doi:[10.1016/j.powtec.2011.11.046](https://doi.org/10.1016/j.powtec.2011.11.046).
- [32] Y. Ichikawa, K. Ogawa, Effect of substrate surface oxide film thickness on deposition behavior and deposition efficiency in the cold spray process, *J. Therm. Spray Technol.* 24 (2015) 1269–1276, doi:[10.1007/s11666-015-0299-y](https://doi.org/10.1007/s11666-015-0299-y).
- [33] M. Hassani-Gangaraj, D. Veysset, K.A. Nelson, C.A. Schuh, Impact-bonding with aluminum, silver, and gold microparticles: toward understanding the role of native oxide layer, *Appl. Surf. Sci.* 476 (2019) 528–532, doi:[10.1016/j.apsusc.2019.01.111](https://doi.org/10.1016/j.apsusc.2019.01.111).
- [34] D. Veysset, A.J. Hsieh, S. Kooi, A.A. Maznev, K.A. Masser, K.A. Nelson, Dynamics of supersonic microparticle impact on elastomers revealed by real-time multi-frame imaging, *Sci. Rep.* 6 (2016) 1–7, doi:[10.1038/srep25577](https://doi.org/10.1038/srep25577).
- [35] J.T. Kloprogge, L.V. Duong, B.J. Wood, R.L. Frost, XPS study of the major minerals in bauxite: gibbsite, bayerite and (pseudo-)boehmite, *J. Colloid Interface Sci.* 296 (2006) 572–576, doi:[10.1016/j.jcis.2005.09.054](https://doi.org/10.1016/j.jcis.2005.09.054).
- [36] B.R. Strohmeier, An Esca method for determining the oxide thickness on aluminum-alloys, *Surf. Interface Anal.* 15 (1990) 51–56, doi:[10.1002/sia.740150109](https://doi.org/10.1002/sia.740150109).
- [37] E. Mittemeijer, C. Borsboom, L.P. Jeurgens, F. Tichelaar, W. Sloof, Determination of thickness and composition of aluminium-oxide overlayers on aluminium substrates, *Appl. Surf. Sci.* 144–145 (2002) 11–15, doi:[10.1016/s0169-4332\(98\)00755-7](https://doi.org/10.1016/s0169-4332(98)00755-7).
- [38] K. Shimizu, K. Kobayashi, G.E. Thompson, G.C. Wood, The apparent induction period for $\gamma\text{-Al}_2\text{O}_3$ development in thermal oxide films on aluminium, *Oxid. Met.* 36 (1991) 1–13, doi:[10.1007/BF00938453](https://doi.org/10.1007/BF00938453).
- [39] K. Shimizu, R.C. Furneaux, G.E. Thompson, G.C. Wood, A. Gotahr, K. Kobayashi, Erratum: on the nature of “Easy Paths” for the diffusion of oxygen in thermal oxide films on aluminum, *Oxid. Met.* 36 (1991) 505, doi:[10.1007/BF01151595](https://doi.org/10.1007/BF01151595).
- [40] B.C. Bunker, G.C. Nelson, K.R. Zavadil, J.C. Barbour, F.D. Wall, J.P. Sullivan, C.F. Windisch, M.H. Engelhardt, D.R. Baer, Hydration of passive oxide films on aluminum, *J. Phys. Chem. B* 106 (2002) 4705–4713, doi:[10.1021/jp013246e](https://doi.org/10.1021/jp013246e).
- [41] C. Dyer, P.J. Hendra, W. Forsling, M. Ranheimer, Surface hydration of aqueous $\gamma\text{-Al}_2\text{O}_3$ studied by Fourier transform Raman and infrared spectroscopy. I. Initial results, *Spectrochim. Acta Part A Mol. Spectrosc.* 49 (1993) 691–705, doi:[10.1016/0584-8539\(93\)80092-O](https://doi.org/10.1016/0584-8539(93)80092-O).
- [42] T. Shirai, J.W. Li, K. Matsumaru, C. Ishizaki, K. Ishizaki, Surface hydration states of commercial high purity $\alpha\text{-Al}_2\text{O}_3$ powders evaluated by temperature programmed desorption mass spectrometry and diffuse reflectance infrared Fourier transform spectroscopy, *Sci. Technol. Adv. Mater.* 6 (2005) 123–128, doi:[10.1016/j.stam.2004.11.003](https://doi.org/10.1016/j.stam.2004.11.003).
- [43] J.T. Kloprogge, H.D. Ruan, R.L. Frost, Thermal decomposition of bauxite minerals: infrared emission spectroscopy of gibbsite, boehmite and diasporite, *J. Mater. Sci.* 37 (2002) 1121–1129, doi:[10.1023/A:1014303119055](https://doi.org/10.1023/A:1014303119055).
- [44] J. Vlcek, L. Gimeno, H. Huber, E. Lugscheider, A systematic approach to material eligibility for the cold-spray process, *J. Therm. Spray Technol.* 14 (2005) 125–133, doi:[10.1361/10599630522738](https://doi.org/10.1361/10599630522738).
- [45] M. Hassani-Gangaraj, D. Veysset, V.K. Champagne, K.A. Nelson, C.A. Schuh, Response to Comment on “Adiabatic shear instability is not necessary for adhesion in cold spray”, *Scr. Mater.* 162 (2019) 515–519, doi:[10.1016/j.scriptamat.2018.12.015](https://doi.org/10.1016/j.scriptamat.2018.12.015).
- [46] N. Bay, Cold Pressure Welding - the Mechanisms Governing Bonding, *ASME Pap.* 101 (1978) 121–127.